Transition between amplitude-modulated and ferrimagnetic states in Ca 3 Co 2 O 6

Vincent Hardy, Martin Lees, Oleg Petrenko

Transition between the Amplitude-Modulated and Ferrimagnetic States in $Ca_3Co_2O_6$

V. Hardy[a], M. R. Lees[b] and O. A. Petrenko[b]

[a] *Université de Caen Normandie, ENSICAEN, CNRS UMR 6508, CRISMAT, Normandie Univ., 14000 Caen, France*

[b] *Department of Physics, University of Warwick, Coventry, CV4 7AL, United Kingdom*

Abstract

$Ca_3Co_2O_6$ is the archetype of a ferromagnetic 1D Ising compound having antiferromagnetically coupled chains distributed on a triangular lattice. In this paper, we investigate a first-order transition, not detected previously, which takes place along the transformation from the spin-density-wave to the ferrimagnetic state. This $T^*(H)$ line has been derived from magnetization and specific heat measurements recorded vs T and vs H, with the magnetic field applied along the anisotropy axis on a set of single crystals. The entropy jump ΔS at the transition has been derived from both the specific heat and magnetization data. A direct link between ΔS and the period of the underlying spin modulations in the SDW state has been established. All the results about $T^*(H)$ are compared to the recent theoretical predictions of Kamiya [PRB **107**, 134409 (2023)], and the degree of consistency was evaluated from the derived values of the magnetic interactions. Comparisons to similar transitions in related materials are also discussed.

Low dimensionality and frustration are two longstanding issues in magnetism. $Ca_3Co_2O_6$ is a compound combining both these aspects which has been the subject of numerous studies over the last twenty years [1-26]. It is a system of spin chains distributed on a perfect triangular lattice, with antiferromagnetic (AF) interchain coupling. These spins are quite large (~ $5\mu_B$) and they have a marked Ising character. It was gradually realized that the geometrical frustration in this material is not only between the chains, but also along each of them, due to helical couplings via neighboring chains, [10,14,16] which compete with the direct intrachain coupling. $Ca_3Co_2O_6$ displays a wide variety of spectacular behaviors, which have made it a rich subject of study. Among these unusual properties, we cite the presence of regularly spaced steps in the magnetization curves at low temperature [4,5,8], the existence of an incommensurate amplitude modulated structure below T_N in zero-field [14-16], and a slow dynamics leading to a time-dependent multiphasic state within a substantial part of the phase diagram [6,18-20,23,24,27].

The present paper reports a new feature that had escaped the previous investigations of $Ca_3Co_2O_6$. It is a sharp first-order transition line, placed in the phase diagram between the spin-density wave (SDW) and ferrimagnetic (FR) regimes, and which turns out to be in remarkable agreement with a recent theoretical prediction formulated by Kamiya [28]. Here, this transition

is carefully tracked by magnetization and specific heat measurements on single crystals. After determining the position of this phase boundary, we discuss its origin on the basis of Ref. [28] and of the general behavior expected for a field-induced transition between SDW and FR states. We emphasize that the existence of both these states was already well known in the literature on $Ca_3Co_2O_6$, and the novelty of our report is the experimental evidence of a well-defined transition line between them. The main features of our compound are the incommensurate nature of its modulated structure, and the fact that there are three types of chains on the triangular network. It is also shown that measurements and calculations of the entropy jump at the transition can help to shed light on the nature of such a type of the transition.

The structure of $Ca_3Co_2O_6$ consists of CoO_6 chains separated by Ca atoms. Each chain is made of an alternation between Co^{3+} in an octahedral environment (leading to a low-spin $S = 0$ state) and Co^{3+} in trigonal prisms (leading to high-spin state, $S = 2$). The latter incorporates a substantial orbital moment and yields a large anisotropy. In practice, $Ca_3Co_2O_6$ (below its $T_N \sim$ 24 K) can be regarded as a pure Ising compound, with individual spin moments close to $5\mu_B$ that are aligned along the chain direction (c axis). These chains are arranged on a triangular lattice and separated by a distance of 5.24 Å, but one must also take into account the existence of a shift along c in the position of the Co between adjacent chains. Actually, if one considers a chain as the center of an hexagon, its six neighboring chains alternate between a first family shifted by $c/6$ (with c = 10.36 Å) along c and a second family shifted by $c/3$ (see [29]). This corresponds to the labels A, B, C in Ref. [20], and to the three colors shown in the bottom inset of Fig.1.

In $Ca_3Co_2O_6$, the largest spin coupling J_1 is the intrachain one, and it is ferromagnetic. The shift described above allows one to distinguish two interchain couplings, namely J_2 between closest spins (5.52 Å) and J_3 between more distant ones (6.27 Å). Each spin is coupled to six spins in neighboring chains by J_2 and to six other spins by J_3 (see [29]). Since these interchain couplings are AF, the triangular topology induces geometrical frustration. This *lateral* (or interchain) geometrical frustration plays a leading role in understanding the global magnetic response when each chain can be regarded as a *giant macrospin*, i.e. at low-T [12,30-33]. But, the situation is markedly different in the high-T range, i.e. just below the magnetic ordering at T_N, as was first shown by Agrestini *et al*. [14]. The present topology, indeed, induces the striking feature that each spin interacts with its two intrachain neighbors via complex paths through neighboring chains [10,14,16,28] (either three times J_2 or twice J_2 plus J_3) (see [29]). These couplings compete with the intrachain ferromagnetic coupling J_1, and since we have Ising spins, this *longitudinal* (intrachain) geometrical frustration leads to an amplitude-

modulated spin ordering. Several authors reported a sine-wave modulation [14,21], while others proposed a squared-up structure [18,27]. In all cases, it was found that this SDW order has a long period of the order of 1000 Å, and is incommensurate. The lower inset of Fig. 1 illustrates schematically the sine-modulated order with the phase shift between the three types of chains.

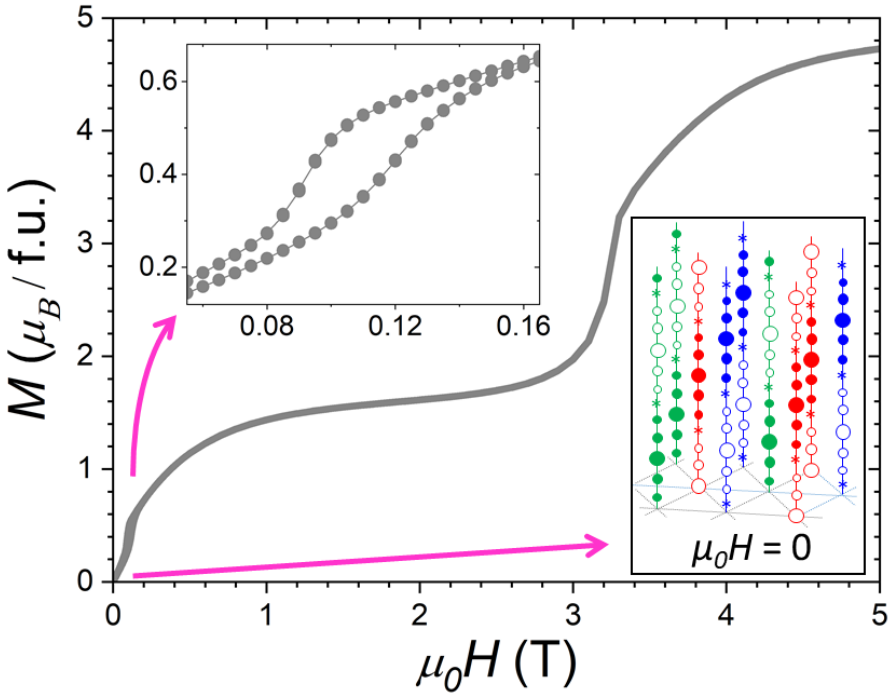

Figure 1: Isothermal magnetization curve recorded at 18 K (main panel). The top inset is an enlargement of the low-field range, showing the signature of the transition under study. The bottom inset is a schematic picture of the spin structure in zero-field (the period shown is much shorter than the real one which involves about one thousand spins). The chains are distributed on a triangular lattice; there are three categories (marked here by different colors) which are distinguished by their positioning along *c*. To illustrate the sinusoidally modulated structure, the size of the circles varies with the amplitude of the spins; these circles are filled or empty for spin up or down, respectively (the crosses correspond to an amplitude equal to zero).

The main panel of Fig. 1 shows the magnetic response in an applied field at 18 K, a temperature between T_N and the low-T regime where the behavior is then characterized by the appearance of equally spaced steps in $M(H)$ (a strongly out of equilibrium effect, that is not addressed in the present letter). The spin system starts from a SDW at $H = 0$, passes through a ferrimagnetic plateau before finally switching towards a saturated magnetization ($M_{sat} \sim 5\mu_B$/f.u at a field $\mu_0 H_{sat}$ whose low-T value is ~ 3.6 T (see [29]). The plateau is centered around $M_{sat}/3$, as expected for two chains "up", one chain "down" (UUD). However, there is an additional, barely visible feature in the low-field range, which was missed to date. In the enlargement shown in the top panel, one observes the presence of a step on each branch of the cycle, with hysteresis leading to a bubble-like shape. This is the transition that is addressed in the present

paper and whose determination has been derived from magnetization and heat capacity measurements.

The sample used in this study is a bunch of needle-like crystals co-aligned along the *c* axis, that were grown following the method described in Ref. [9]. This assembly roughly forms a cylinder of length 4 mm and diameter 0.9 mm. Such an aspect ratio is convenient for magnetic measurement in the H // c orientation, and one just needs enough resolution to reveal the steps; for this purpose, we used a sweep rate of 0.2 K /min for the $M(T)$ and 5 mT spaced data points for the $M(H)$ measurements. These magnetization measurements were recorded in a Quantum Design MPMS3 magnetometer. Performing specific heat measurements with H // c is challenging with a vertical field and a horizontal platform, as is the usual case in most calorimeters. We made use of the Quantum Design Physical Property Measurement System (semi-adiabatic technique) equipped with a *vertical* puck, allowing us to roughly place the sample with H // c [34]. Then, to optimise the orientation, the sample pasted on with Apiezon N grease is slowly cooled from room temperature to ~ 100 K (i.e. below the freezing temperature of the grease) in our highest field of 9 T. The magnetic torque forces the H // c orientation, while the sample is progressively blocked into the grease. The magnetic field is then zeroed at 100 K, and the sample can follow a zero-field-cooled preparation. Another difficulty with the specific heat measurements is that one deals with a first-order transition, as already shown in Fig. 1. This means that one must use a single pulse method to record meaningful $C(T)$ data [35,36]. A temperature pulse spanning the width of the transition is applied and a time-resolved analysis of the thermal response is performed (see [29]), as described in previous studies [36-38]. For the $C(B)$ measurements, the standard 2τ method must be used; even though it cannot give access to the latent heat, it is sufficient to locate the transition.

Examples of these various types of measurements are collected in Fig. 2. Magnetization data exhibit the same type of signatures in both $M(T)$ and $M(H)$, and the transition values of temperature or field are derived from the inflection points (see [29]). From linear approximations of the curve on each side of the transition, one can also estimate the step ΔM by considering the shift between these two extrapolations at the level of the midpoint transition. In the $C(T)$ curves, one can detect in the same pulse the signature of T_N (virtually the same for warming and cooling) and that of the transition under study (which exhibits marked hysteresis). To precisely derive the location of these peaks –and the associated excess heat capacity– one considers the field-dependent baseline obtained from standard measurement with the 2τ method

(see [29]). This curve includes a false peak at the transition that must be removed to build the baseline curve [see Fig. 2(c)]. As often encountered in first-order transitions, the background heat capacity (i.e. without the latent heat component) is slightly modified at the transition, leading to a ΔC between the two sides of the $C(T)$. This feature can be more easily detected in the $C(H)$ curves, as shown in Fig. 2(d). The change is small, but this is a clearly defined step which allows the transition fields to be determined.

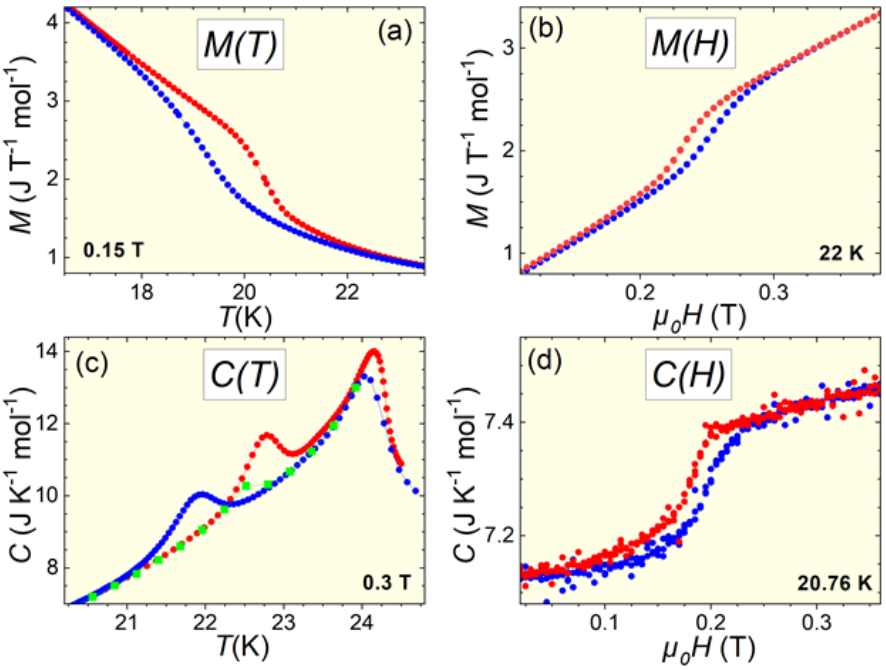

Figure 2: Illustrations of the four types of measurements performed to derive the transition line. The red curves correspond to the warming or field-decreasing measurements, while the blue curves correspond to the cooling or field-increasing measurements. The results of the standard 2τ measurements (green squares) are also shown in panel (c). The transition temperatures or transition fields were derived from the inflection points in the *M(T)*, *M(H)* and *C(H)* curves, whereas they were ascribed to the locations of the peaks in the case of *C(T)* data.

On the basis of these different measurements, we derived the location of the transition in the (*H, T*) phase diagram (see [29] for details about the methods and criteria used). Actually, it is a pair of lines, depending on the sense of crossing: in the present case, there is an equivalence between increasing temperature and decreasing the field, as well as between decreasing temperature and increasing the field. All the results are reported in Fig. 3, and one observes a satisfying overall consistency between the various sets of data. Nevertheless, the curve derived from $C(T)$ upon cooling (stemming from the return branch of the temperature pulse) stands apart from the others. This is not just a matter of thermometry since the $C(T)$ upon warming and the $C(B)$ data are consistent with each other and with the magnetization data. It is instead a feature originating from the fast dynamics of this type of measurement, which corresponds to about 0.15 K/s (i.e. temperature changes about 50 times faster than for the M vs. T). The first

phenomenon to be considered is the unavoidable shift between the measured temperature (i.e. that of the platform) and that of the sample itself (cf. [29]). The thermal equation of the sample in this device leads to $T_p - T_s = [P - C_{ad}(dT_p/dt) - K_w(T_p - T_0)]/K_g$, where T_p and T_s are the platform and sample temperature respectively, K_g is the thermal conductivity of the layer of grease, K_w that of the wires in between the platform and the base at temperature T_0, P is the heating power applied to the platform and C_{ad} is the heat capacity of the platform plus grease. This yields a correction which can differ for the two branches of the pulse and is thus able to induce an effect such as the one observed. From an estimate of $K_g \sim 2250$ W/K (cf. [29]) T_p - T_s is found to be ~ 0.02 and 0.03 K for the warming and cooling data, respectively, at the level of the transition. Clearly, this experimental correction cannot account for the observed shift of the curve built from $C(T_{cooling})$ data. There is likely another, more fundamental effect of the dynamics which impacts differently on the transition upon cooling and warming. This deserves further investigation, but is beyond the scope of the present study.

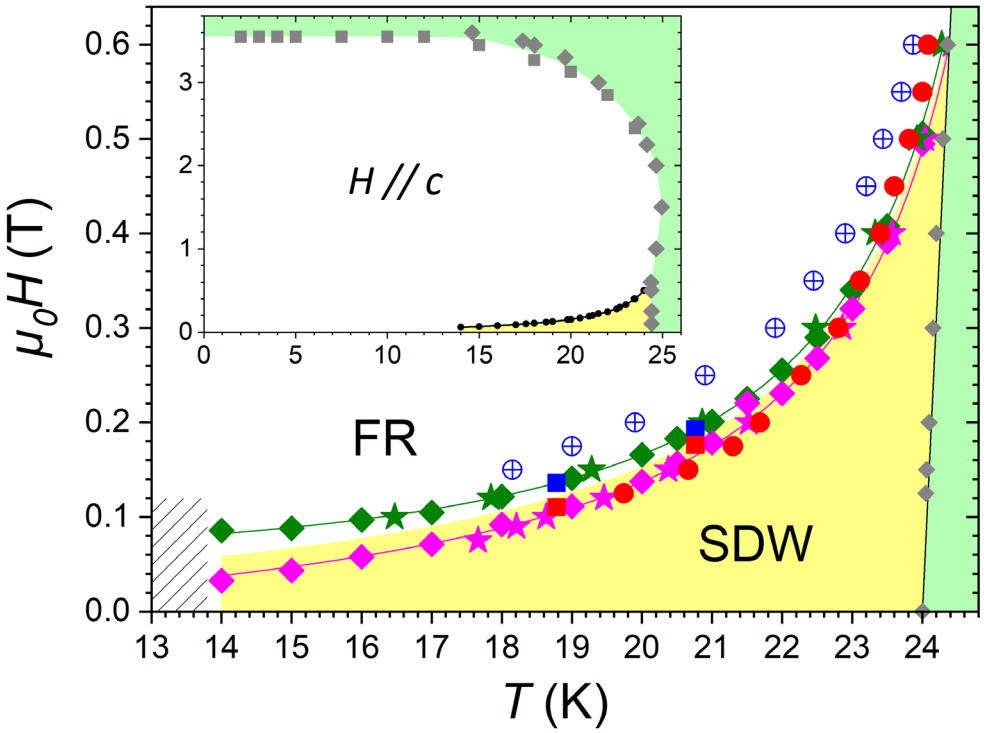

Figure 3: Phase diagram of $Ca_3Co_2O_6$. The main panel focuses on the $T^*(H)$ transition found between the SDW and FR states. Various types of measurements were used to locate this transition :$C(T_{warming})$ (●), $C(T_{cooling})$ (⊕), $C(H_{increasing})$ (■), $C(H_{decreasing})$ (■), $M(T_{warming})$ (★), $M(T_{cooling})$ (★), $M(H_{increasing})$ (◆), $M(H_{decreasing})$ (◆). The black line connecting the gray diamonds marks the $T_N(H)$. The top panel is an extended phase diagram including the $H_{sat}(T)$ line (gray squares) marking the field-induced transition towards saturated paramagnetism. The line made of black circles in this inset shows the "mean" *H*(T)* line corresponding to the upper boundary of the yellow area in the main panel.

As visible in Fig. 3, the transition line exhibits a very particular shape, being almost vertical at higher temperatures and nearly horizontal at lower temperatures. Even though the crossing with $T_N(H)$ is subtle since the two lines connect tangentially, one can estimate that this crossing takes place close to 24.2 K and 0.6 T. Owing to its shape, the determination of this line is more convenient with measurements versus T in higher fields, and with measurements versus H at lower temperatures. We checked experimentally that the low-T part of the line is difficult to derive from measurements versus T, both for $M(T)$ and $C(T)$ (see [29]). One also approaches the detection threshold of the $C(H)$ technique, since the overall heat capacity decreases as T is reduced. So the most suitable approach at low-T is clearly provided by the $M(H)$ curves. By recording such data down to 10 K with 1 K-steps, one observes a sudden change of behavior around 13 K; below this temperature, there is still an open hysteresis loop, but the shapes of the two branches are different (see [29]). The existence of such a crossover in temperature agrees with several results in the literature [6,7,15,18,19,23,27,39], in particular those based on neutron diffraction data. In References [18] and [19] for instance, it is reported that the SDW state starts to become destabilized below 13 K: the magnetization becomes strongly time-dependent and several magnetic phases start competing with the SDW order. For this reason, we limit ourselves hereafter to temperatures above 13 K. The transition lines are obtained by aggregating the points derived from $M(H)$, $M(T)$, $C(H)$ and $C(T)$ data, for either $H_{decreasing}/T_{warming}$ or $H_{increasing}/T_{cooling}$ (just discarding the heat capacity for the latter category). A phenomenological fitting to these data (see [29]) is shown as full lines in Fig. 3. In the following, we also consider the mean line denoted as $T^*(H)$ or $H^*(T)$.

On the more complete phase diagram (top panel of Fig. 3), one sees that $T^*(H)$ actually delimits a small area lying in between the SDW and FR regimes, while its shape and location are consistent with the boundary predicted by Kamiya [28]. It is thus very tempting to simply ascribe the boundary to the SDW/FR transition. However, one observes in Fig. 1 that the transition clearly takes place below the FR plateau, since the magnetization above the step remains considerably smaller than $M_{sat}/3$. The nature of $T^*(H)$ is thus probably more complex than expected. One notes that the neutron-diffraction studies of the zero-field SDW concluded that the maximum values of the individual spins are equal to the expected full spin moment, i.e. about $5\mu_B$. So, application of the field is expected to reduce the amplitude of the incommensurate modulation, keeping the same maximum moment along the field direction, while gradually increasing a $\mathbf{q} = 0$ component (see [29]), in a way similar to what has been observed in the incommensurate amplitude-modulated antiferromagnet $PrNi_2Si_2$ [40,41]. This would lead an UUD order yielding an overall magnetization that increases with the magnetic

field, in accordance with observations. At this stage, a possibility to account for the magnetization value found above the transition is to consider that one reaches a "ferrimagnetic" state (i.e. UUD without modulation) that is *non-saturated*, i.e. with a magnetization on each chain lower than M_{sat} (see [29]). Then, it is only the application of higher magnetic field that would progressively polarize this FR state and finally reach the canonical $M_{sat}/3$ value. Further diffraction experiments would be necessary to directly address such a scenario.

Given the intense work devoted to $Ca_3Co_2O_6$ ober the last twenty years, it may seem surprising that this transition line has not been reported before. Kamiya only identified two studies whose results could be related to the predictions in [28]. The first is a μSR experiment that exhibits a change of regime around 0.4 T for 20 K [42]; the second is a study of the magnetocaloric effect, showing an inflection point in the field dependence of the isothermal entropy change (this anomaly draws in the *H-T* plane a line located around 0.1-0.2 T in the range 10-20 K) [23]. In both cases, the agreement with our results is only qualitative, and the first-order aspect of the transition is not reported. Exploring the literature focused on magnetic measurements (likely to show more direct indications of the transition), one can find a few examples of behavior similar to those of the present paper. For instance, in one of the earliest studies on $Ca_3Co_2O_6$, Kageyama *et al.* [3] reported a *M(H)* cycle at 15 K which displays a bubble-like feature in the low-field region when using a slow enough sweep rate. More recently, one observes that the *M(H)* loop at 22 K reported by Hegde *et al.* [25] displays a small anomaly in the low-field range that bears a striking resemblance with our data. In terms of measurements versus temperature, we note that the *M(T)* curve recorded in 0.1 T in one of our first studies exhibits a knee close to 18 K [6]. These scarce hints in magnetic measurements of a transition turn out to be in quantitative agreement with the present data. However, at the time they were obtained, it would have been difficult to claim the existence of a *T*(H)* transition line - such as that seen in the present study- on the basis of this evidence alone.

Complementary information about the nature of *T** can be provided by the value of the latent heat associated to the transition. We previously noted the first-order character of the *T**(*H*) line is manifested by sharp transitions and the presence of hysteresis. Such a type of transition is necessarily accompanied by a change in entropy ascribable to a modification in the degrees of freedom of the spin structures. This change (ΔS) can be evaluated by integration of the excess heat capacity (C_{exc}) that is superimposed onto the background component. We consider hereafter that ΔS is the saturation value of this integration when crossing the whole transition (see [29]). It turns out that ΔS values can also be derived from magnetization by using

the Clausius-Clapeyron equation, $\Delta S = -\Delta M/(\frac{dT^*}{\mu_0 dH})$. For this purpose, we evaluated ΔM as previously described and used a phenomenological fitting of $T^*(H)$ (see [29]). In this way one obtains values in good agreement with those deduced from $C(T)$. The ΔS values are reported as a function of T in the bottom inset of Fig. 4. First, it must be realized that these values are quite small; when expressed in entropy per spin, one reaches maximal values of ~ 0.007 k_B per spin close to T_N. Second, one observes that this entropy step tends to vanish as the temperature is reduced; this small signal likely contributes to the difficulty encountered in the determination of the line in the low-T range.

ΔS at the SDW/FR transition can also be calculated from the decrease in degrees of freedom resulting from the disappearance of the modulation along the chains. Let us consider the minimal set of spins required to describe both the SDW and FR phases, namely three neighboring chains (belonging to the A, B, C types) along which one considers the number of spins corresponding to the period of the modulation (denoted N). This geometry is shown in the upper inset of Fig. 4 with spins shown perpendicular to the chain for the sake of clarity (rather than parallel to the field, as they actually are). Then, one has to estimate the number of possible configurations for such a set of $3N$ spins, denoted W. In the SDW regime, there are three possibilities for the choice of the "down" chain, and N for the position of the wave on the first chain, leading to $W_{SDW} = 3N$. In the FR state, there is only the choice of the "down" chain, yielding $W_{FR} = 3$. The entropy per spin is $s = k_B (\ln W)/3N$ and the molar entropy difference, $\Delta S = N_A (s_{SDW}\text{-}s_{FR})$, where N_A is the Avogadro number. Introducing the molar gas constant ($R = k_B N_A$), one arrives at the expression $\Delta S = (R/3N) \ln N$, that is plotted in Fig. 4. It is worth emphasizing that we thereby obtain a direct link between the experimental values of ΔS and the underlying N value. In magnetic fields approaching ~ 0.5 T, T^* becomes close to T_N. In this regime, one gets the highest value of ΔS ~ 0.06 J K^{-1} mol^{-1} which is found to correspond to N ~ 250. Note that this evaluation is also relevant to the zero-field SDW state (at the same T^*), since there is no field-dependence in our estimate of S. It can thus be compared to the zero-field neutron experiments which reported N values of about 200 just below T_N [14]. Therefore, we observe a remarkable agreement between these two approaches (neutron diffraction and entropy measurements). At lower temperature, we see in Fig. 4 that one gets a smaller ΔS, and this corresponds to larger N values, of the order of 1000. Such an evolution is consistent with the qualitative variation claimed in the x-ray diffraction experiments [15]. The present ΔS approach has the advantage to facilitate the quantification of this T dependence of N.

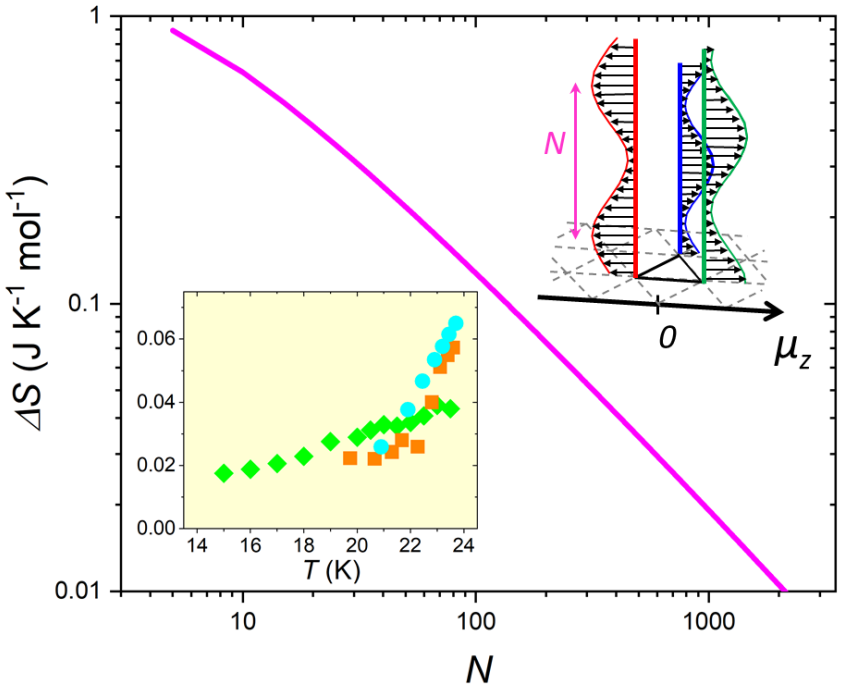

Figure 4: Calculation of the entropy change at the SDW-to-FR transition as a function of the period of the modulated state expressed in number N of adjacent spins (thick magenta line). This parameter is shown in the top inset, which also illustrates the spin state in an intermediate field (μ_z is the spin value, being positive if oriented along the same direction as the field); among a set of three chains belonging to the A, B, C categories, two of them yield an overall magnetization "up" while the third is "down" (note that the spins are drawn perpendicular to the chains while they are actually oriented along them). The bottom inset shows the experimental values of the entropy jump at the $T^*(H)$ line derived from different types of measurements: $C(T_{warming})$ (■), $C(T_{cooling})$ (●), and $M(H)$ (◆).

Let us now compare in more detail the $T^*(H)$ line to Kamiya's predictions [28]. Qualitatively speaking, the theoretical line is very similar to the experimental one: it has the same position in the phase diagram, it exhibits a positive dH^*/dT slope, there is a multicritical point at the crossing between $T^*(H)$ and $T_N(H)$, and the line seems to vanish around $T_N/2$ in zero-field. Within the framework of the $-k_B J \sigma_i \sigma_j$ convention for the interaction Hamiltonian (where σ_k is ± 1, depending on whether the spin direction at the site k is parallel or antiparallel to H // c), and considering the reduced field $h = g\mu_B S\mu_0 H$ (where $gS\mu_B$ is the saturation moment), the multicritical point reported by Kamiya corresponds to:

$$T^*/J_1 = 1.4 \quad (1a) \qquad \text{and} \qquad h^*/k_B J_1 = 0.2 \quad (1b)$$

Experimentally, we found T^* = 24.2 K and $\mu_0 H^*$ = 0.6 T. First, it should be noted that our H^* value is consistent with the transition field to saturated paramagnetism at low-T, i.e. $\mu_0 H_{sat}$ = 3.6 T. Indeed, one recovers the factor ~ 6 between these values that was predicted in Kamiya's model ($h_{sat}/k_B J_1 = 1.2$). Second, one can go a step further in the quantitative analysis by calculating the J_1 value derived from (T^*, H^*). Equation 1(a) leads to $J_1 = 17.3$ K,

while Eq. 1(b) yields J_1 = 10.5 K. These two values are clearly of the same order of magnitude, but are still different.

Let us now compare these values with estimates of J_1 derived from other approaches. For the sake of clarity, hereafter, we convert the results of the literature to the convention adopted by Kamiya ($-k_B J \sigma_i \sigma_j$). Measuring the magnetic susceptibility $\chi(T)$ on a polycrystalline sample, J_1 is directly given by the Curie-Weiss temperature θ_{CW} (when neglecting the secondary interactions). This led to 28 K [2] or 40 K [3]. From the magnetic susceptibility measured with H // c in oriented samples, values of 30 K [4] and 52 K [43] were reported. Different models were used in these studies, and it must be emphasized that the analysis of χ // c in Ising-like compounds is made complex by the interplay between the interaction and anisotropy parameters, leading to estimates of J_1 that are very model-dependent. In another study involving a set of $\chi(T)$ data measured in a ceramic sample and in a crystal with H // c and $H \perp c$, a value $J_1 \sim 36$ K was derived [13]. Other measurements can also give access to J_1: recently, independent studies of nuclear magnetic resonance [22] and polarized-neutron diffraction [24] led to the same value of 24 K.

It must be underlined that the secondary interactions J_2 and J_3 have been neglected in most of the previous magnetic studies, even though they are not that much smaller than J_1. These couplings are directly related to the transition field towards saturation by the relationship $h_{sat} = 6k_B(J_2 + J_3)$. From the value $\mu_0 H_{sat}$ = 3.6 T combined with M_{sat} = 5.2 μ_B [17,18,25], one obtains $J_2 + J_3$ = 2.1 K. This value is close to the 2.3 K derived by Allodi *et al.* [22] from nuclear magnetic resonance experiments. Incorporating the results of a one-dimensional Ising approximation, these authors found $J_2 \sim 1.1$ K, leading to $J_3 \sim 1.2$ K. Introducing these interchain couplings in the mean-field analysis of θ_{CW}, the J_1 evaluated from the data of Ref. [13] for instance is shifted from 36 to 30 K. To sum up, it can be stated that the most reliable estimates of J_1 lie in the range (24-30 K). There is therefore a small but real shift compared to the values derived from the Kamiya's formula, i.e. (10-17 K). In other words, the agreement between the experimental $T^*(H)$ line and the Kamiya's predictions is excellent from a qualitative viewpoint, but it is only semi-quantitative.

Let us now enlarge the scope to other materials susceptible to exhibit the same type of transition. $PrNi_2Si_2$ is a well-known example of an incommensurate amplitude-modulated AF structure [40,41]. Application of a magnetic field leads to a gradual decrease of the incommensurate modulation amplitude, with a critical field corresponding to the disappearance of the modulations. The signatures in the $M(H)$ curves are similar to those observed in

$Ca_3Co_2O_6$, but the situation remains different in that one deals with a metamagnetic transition from AF to saturated paramagnetism in $PrNi_2Si_2$, not towards ferrimagnetism. Another related compound is $CoNb_2O_6$, which is actually closer to our case since it is a Ising spin chain compound with an isosceles triangular geometry [44,45]. Moreover, this material exhibits a first-order transition from a sinusoidally amplitude-modulated incommensurate phase to a FR phase, i.e. a behavior comparable to what we observe. The shape of the line in the phase diagram is also similar to ours, showing a positive dH^*/dT slope and a multicritical point. However, it was observed that –for some unknown reasons- the transition is only detectable when the field is decreased, not when it increases; moreover, no connection between this line and the coupling constants has been reported to the best of our knowledge. It thus appears that $Ca_3Co_2O_6$ can significantly complement the phenomenology of the SDW-to-FR transition.

In summary, a new transition line has been identified and discussed in $Ca_3Co_2O_6$, which is the archetype of a ferromagnetic Ising 1D spin chain compound with a triangular lattice. This is a first-order transition between two phases previously established in $Ca_3Co_2O_6$, namely spin-density-wave and ferrimagnetic phases. The associated entropy change is consistent with previous evaluations of the spin period in the amplitude-modulated state. Specific neutron diffraction experiments are now required to clarify the exact nature of the two phases around the transition. These data are not yet available despite the abundant literature on this compound because it will require an investigation of a very specific region of the phase diagram, delimited by magnetic fields of 0.1 - 0.6 T in the temperature range 14 - 24 K.

---

[1] H. Fjellvåg, E. Gulbrandsen, S. Aasland, A. Olsen, and B. C. Hauback, Crystal Structure and Possible Charge Ordering in One-Dimensional $Ca_3Co_2O_6$, J. Solid State Chem. **124**, 190 (1996).

[2] S. Aasland, H. Fjellvåg, B. Hauback, Magnetic properties of the one-dimensional $Ca_3Co_2O_6$, Solid State Commun. **101**, 187 (1997).

[3] H. Kageyama, K. Yoshimura, K. Kosuge, H. Mitamura, T. Goto, Field-induced magnetic transitions in the one-dimensional compound $Ca_3Co_2O_6$, J. Phys. Soc. Jpn. **66**, 1607 (1997).

[4] H. Kageyama, K. Yoshimura, K. Kosuge, M. Azuma, M. Takano, H. Mitamura, and T. Goto, Magnetic Anisotropy of $Ca_3Co_2O_6$ with Ferromagnetic Ising Chains, J. Phys. Soc. Jpn. **66**, 3996 (1997).

[5] A. Maignan, C. Michel, A.-C. Masset, C. Martin and B. Raveau, Single crystal study of the one dimensional $Ca_3Co_2O_6$ compound: five stable configurations for the Ising triangular lattice, Eur. Phys. J. B **15**, 657 (2000).

[6] V. Hardy, S. Lambert, M. R. Lees, D.M. Paul, Specific heat and magnetization study on single crystals of the frustrated quasi-one-dimensional oxide $Ca_3Co_2O_6$, Phys. Rev. B **68**, 014424 (2003).

[7] E. Sampathkumaran, N. Fujiwara, S. Rayaprol, P. Madhu, Y. Uwatoko, Magnetic behavior of Co ions in the exotic spin-chain compound $Ca_3Co_2O_6$ from Co 59 NMR studies, Phys. Rev. B **70**, 014437 (2004).

[8] V. Hardy, M. R. Lees, O. A. Petrenko, D.M. Paul, D. Flahaut, S. Hébert, A. Maignan, Temperature and time dependence of the field-driven magnetization steps in $Ca_3Co_2O_6$ single crystals, Phys. Rev. B **70**, 064424 (2004).

[9] V. Hardy, D. Flahaut, M. R. Lees, O. A. Petrenko, Magnetic quantum tunneling in $Ca_3Co_2O_6$ studied by ac susceptibility: Temperature and magnetic-field dependence of the spin-relaxation time, Phys. Rev. B **70**, 214439 (2004).

[10] R. Frésard, C. Laschinger, T. Kopp, and V. Eyert, Origin of magnetic interactions in $Ca_3Co_2O_6$, Phys. Rev. B **69**, 140405(R) (2004).

[11] O. A. Petrenko, J. Wooldridge, M. R. Lees, P. Manuel, and V. Hardy, Single crystal neutron diffraction study of the magnetisation process in $Ca_3Co_2O_6$, Eur. Phys. J. B. **47**, 79 (2005).

[12] Y. B. Kudasov, Steplike Magnetization in a Spin-Chain System: $Ca_3Co_2O_6$, Phys. Rev. Lett. **96**, 027212 (2006).

[13] V. Hardy, D. Flahaut, R. Frésard and A. Maignan, Anisotropic susceptibility of the geometrically frustrated spin-chain compound $Ca_3Co_2O_6$, J. Phys. Condens. Matter **19**, 145229 (2007).

[14] S. Agrestini, L. Chapon, A. Daoud-Aladine, J. Schefer, A. Gukasov, C. Mazzoli, M. R. Lees, O. A. Petrenko, Nature of the Magnetic Order in $Ca_3Co_2O_6$, Phys. Rev. Lett. **101**, 097207 (2008).

[15] S. Agrestini, C. Mazzoli, A. Bombardi, M. R. Lees, Incommensurate magnetic ground state revealed by resonant x-ray scattering in the frustrated spin system $Ca_3Co_2O_6$, Phys. Rev. B **77**, 140403 (2008).

[16] L. Chapon, Origin of the long-wavelength magnetic modulation in $Ca_3Co_2O_6$, Phys. Rev. B **80**, 172405 (2009).

[17] C. Fleck, M. R. Lees, S. Agrestini, G. McIntyre, O. A. Petrenko, Field-driven magnetisation steps in $Ca_3Co_2O_6$: a single-crystal neutron-diffraction study, Europhys. Lett. **90**, 67006 (2010).

[18] T. Moyoshi, K. Motoya, Incommensurate magnetic structure and its long-time variation in a geometrically frustrated magnet $Ca_3Co_2O_6$, J. Phys. Soc. Jpn. **80**, 034701 (2011).

[19] S. Agrestini, C. Fleck, L. Chapon, C. Mazzoli, A. Bombardi, M. R. Lees, O. A. Petrenko, Slow magnetic order-order transition in the spin chain antiferromagnet $Ca_3Co_2O_6$, Phys. Rev. Lett. **106**, 197204 (2011).

[20] Y. Kamiya, C. Batista, Formation of magnetic microphases in $Ca_3Co_2O_6$, Phys. Rev. Lett. **109**, 067204 (2012).

[21] A. Jain, P. Y. Portnichenko, H. Jang, G. Jackeli, G. Friemel, A. Ivanov, A. Piovano, S. M. Yusuf, B. Keimer, and D. S. Inosov, One-dimensional dispersive magnon excitation in the frustrated spin-2 chain system $Ca_3Co_2O_6$, Phys. Rev. B **88,** 224403 (2013).

[22] G. Allodi, P. Santini, S. Carretta, S. Agrestini, C. Mazzoli, A. Bombardi, M. R. Lees, and R. De Renzi, Exchange interactions in $Ca_3Co_2O_6$ probed locally by NMR, Phys. Rev. B **89**, 104401 (2014).

[23] P. Lampen, N. Bingham, M. Phan, H. Srikanth, H. Yi, S. Cheong, Macroscopic phase diagram and magnetocaloric study of metamagnetic transitions in the spin chain system $Ca_3Co_2O_6$, Phys. Rev. B **89**, 144414 (2014).

[24] J.A. Paddison, S. Agrestini, M.R. Lees, C.L. Fleck, P.P. Deen, A.L. Goodwin, J.R. Stewart, O.A. Petrenko, Spin correlations in $Ca_3Co_2O_6$: polarized-neutron diffraction and Monte Carlo study, Phys. Rev. B **90**, 014411 (2014).

[25] N. G. Hegde, I. Levati´c, A. Magrez, H. M. Rønnow, and I. Živkovic, Magnetic dynamics across the in-field transition in $Ca_3Co_2O_6$, Phys. Rev. B **102**, 104418 (2020).

[26] I. Nekrashevich, X. Ding, F. Balakirev, H. T. Yi, S.-W. Cheong, L. Civale, Y. Kamiya, and V. S. Zapf, Reaching the equilibrium state of the frustrated triangular Ising magnet $Ca_3Co_2O_6$, Phys. Rev. B **105**, 024426 (2022).

[27] K. Motoya, T. Kihara, H. Nojiri, Y. Uwatoko, M. Matsuda, and T. Hong, Time and Magnetic Field Variations of Magnetic Structure in the Triangular Lattice Magnet $Ca_3Co_2O_6$, J. Phys. Soc. Jpn. **87**, 114703 (2018).

[28] Y. Kamiya, Magnetic field induced deformation of the spin density wave microphases in $Ca_3Co_2O_6$, Phys. Rev. B 107, 134409 (2023).

[29] See Supplemental Material at xxx for details about several issues : (1) Interchain shifts along the c axis; (2) Interchain couplings J_2 and J_3; (3) Criteria used to derive the transition fields and temperatures; (4) Time-resolved analysis of the thermal data; (5) Correction of the temperature lag between the platform and the sample; (6) Crossover around 13 K in the magnetic response; (7) Problems with the derivation of T^* from measurements versus T in low fields; (8) Experimental determination of ΔS from specific heat measurements; (9) Experimental determination of ΔS from magnetization measurements; (10) Transition field towards saturation at $T << T_N$; (11) Possible scenario for the field dependence of the SDW state.

[30] X. Y. Yao, S. Dong, and J.-M. Liu, Steplike magnetization of spin chains in a triangular lattice: Monte Carlo simulations, Phys. Rev. B **73**, 212415 (2006).

[31] X. Yao, S. Dong, H. Yu, J. Liu, Monte Carlo simulation of magnetic behavior of a spin-chain system on a triangular lattice, Phys. Rev. B **74**, 134421 (2006).

[32] Y.B. Kudasov, Magnetic structure and phase diagram in a spin-chain system: $Ca_3Co_2O_6$, Europhys. Lett. **78**, 57005 (2007).

[33] Y. B. Kudasov, A. S. Korshunov, V. N. Pavlov, and D. A. Maslov, Dynamics of magnetization in frustrated spin-chain system $Ca_3Co_2O_6$, Phys. Rev. B **78**, 132407 (2008).

[34] PPMS Application Note 1085-156, Quantum Design.

[35] J. C. Lashley, M. F. Hundley, A. Migliori, J. L. Sarrao, P. G. Pagliuso, T. W. Darling et *al.*, Critical examination of heat capacity measurements made on a Quantum Design physical property measurement system. Cryogenics **43**, 369 (2003).

[36] V. Hardy, Y. Bréard, C. Martin, Derivation of the heat capacity anomaly at a first-order transition by using a semi-adiabatic relaxation technique. J Phys:Condens Matter **21**, 075403 (2009).

[37] H. Suzuki, A. Inaba, C. Meingast, Accurate heat capacity data at phase transitions from relaxation calorimetry, Cryogenics **50**, 693 (2010).

[38] A. Scheie, LongHCPulse: Long-Pulse Heat Capacity on a Quantum Design PPMS, J. Low Temp. Phys. **193**, 60 (2018).

[39] H. Kageyama, K. Yoshimura, K. Kosuge, X. Xu, and S. Kawano, Low Temperature Magnetic Phase of Triangular Lattice Antiferromagnet $Ca_3Co_2O_6$, J. Phys. Soc. Jpn. **67**, 357 (1998).

[40] J. A. Blanco, D. Schmitt, and J. C. Gómez-Sal, Metamagnetism and thermodynamical properties systems: modelisation and application to $PrNi_2Si_2$, J. Magn. Magn. Mater. **116**, 128 (1992).

[41] J. A. Blanco, B. Fåk, E. Ressouche, B. Grenier, M. Rotter, D. Schmitt, J. A. Rodríguez-Velamazán, J. Campo, and P. Lejay, Magnetic field and temperature dependence of the amplitude-modulated magnetic structure of $PrNi_2Si_2$ determined by single-crystal neutron diffraction, Phys. Rev. B **82**, 054414 (2010).

[42] S. Takeshita, T. Goko, J. Arai, and K. Nishiyama, J. Phys. Chem. Solids **68**, 2174 (2007).

[43] A. Maignan, V. Hardy, S. Hébert, M. Drillon, M. R. Lees, O. Petrenko, D.M.K. Paul, D. Khomskii, Quantum tunneling of the magnetization in the Ising chain compound $Ca_3Co_2O_6$, J. Mater. Chem. **14**, 1231 (2004).

[44] S. Kobayashi, S. Mitsuda, and K. Prokes, Low-temperature magnetic phase transitions of the geometrically frustrated isosceles triangular Ising antiferromagnet $CoNb_2O_6$, Phys. Rev. B **63**, 024415 (2000).

[45] S. Kobayashi, S. Mitsuda, S. Hosaka, H. Tamatsukuri, T. Nakajima, H. Koorikawa, K. Prokes, and K. Kiefer, Neutron diffraction study of low-temperature magnetic phase diagram of an isosceles-triangular-lattice Ising antiferromagnet $CoNb_2O_6$, Phys. Rev. B **94**, 134427 (2016).

SUPPLEMENTAL MATERIAL

Transition between the Amplitude-Modulated and Ferrimagnetic States in $Ca_3Co_2O_6$

1- Interchain shifts along the *c* axis

There are three families of chains in $Ca_3Co_2O_6$, which only differ by their positioning along the *c* axis. Their distribution on the triangular lattice is shown in Fig. S1(a), where each family is represented by a different color. There is a unique interchain distance *d* (5.24 Å). Adopting, for instance, the A family (red) as the reference, the B family (green) is shifted by *c*/6 along the chain axis (*c* axis), while the C family (blue) is shifted by 2*c*/6 along this same direction.

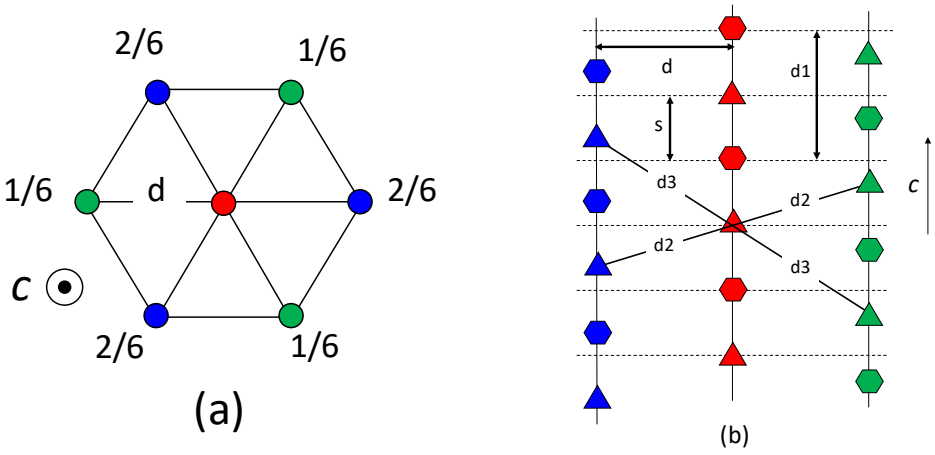

Fig. S1: (a) View along the chain direction (*c* axis). With respect to the central red chain, the green and blue chains are shifted by *c*/6 or *c*/3 along the *c* axis, respectively. (b) View perpendicular to the chains. The triangles and hexagons represent the prismatic and octahedral sites of Co^{3+}, respectively. See text for the meaning of the various distances shown in this panel.

Figure S1(b) shows another illustration of this arrangement by considering a vertical plane (i.e. containing the *c* axis) with three adjacent chains (one of each family). Along each chain, one sees the alternation between the magnetic Co^{3+} prismatic sites, (shown by triangles) and the non-magnetic octahedral sites, (shown by hexagons). The *c* axis lattice parameter amounts to four times the Co separation along the chain, referred to as *s* (2.59 Å); the green chain is shifted by 2s/3 = c/6 with respect to the red one, while the shift is twice as large for the blue chain; the distance between first interchain neighbors is either d_2 (5.52 Å) or d_3 (6.27 Å);

these distances correspond to J_2 and J_3, respectively. As for the intrachain coupling J_1, it corresponds to the distance $d_1 = 2s$ (5.18 Å).

2- Interchain couplings J_2 and J_3

Figure S2 shows a view of three adjacent chains (one of each family) whose repetition constitutes the spin lattice of $Ca_3Co_2O_6$. The symbols and spin positions are the same as in Fig. S1. Considering for instance a spin in chain A, one observes that the coupling with each of these two first intrachain neighbors does not only involve J_1. There are actually two other types of more complex paths, via one or two neighboring chains: the first corresponds to the succession of three J_2 couplings (A→ B→ C→ A or A→ C→ B→ A), and the second is a combination of one J_2 followed by one J_3 (A→ B → A or A→ C→ A).

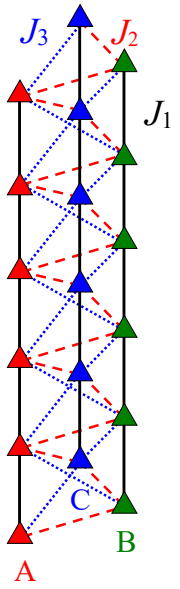

Fig. S2: First neighbors spin interactions (intra- and inter-chains) within a set of three adjacent chains. The symbols and labels are the same as in Fig. S1. Each type of coupling is drawn differently: J_1 (thick black), J_2 (dashed red), J_3 (dotted blue).

3- Criteria used to derive the transition fields and temperatures

For the magnetization data, the values of the transition fields or temperatures were associated to the inflection points of the curves, in other words the points of maximum slope. The same criterion was used for the specific heat data versus field. The situation is different for the specific heat curves versus temperature since in this case the dominant feature at the transition is a peak reflecting the latent heat, that is centered at the transition. We thus simply considered the position of these peaks to derive T^*. In principle, one should consider C_{exc} rather than the total C (i.e., subtract C_{back} from the C curve) but, in practice, we checked it has only a

very tiny effect on the *position* of the peak (in contrast to its *height*), in such a way that the background can be neglected for the determination of the transition positions.

Figure S3 illustrates these methods for each type of measurement. The two transition values in each case are then reported in the phase diagram (bottom panel) allowing one to get an overall picture of the way the transition lines were constructed.

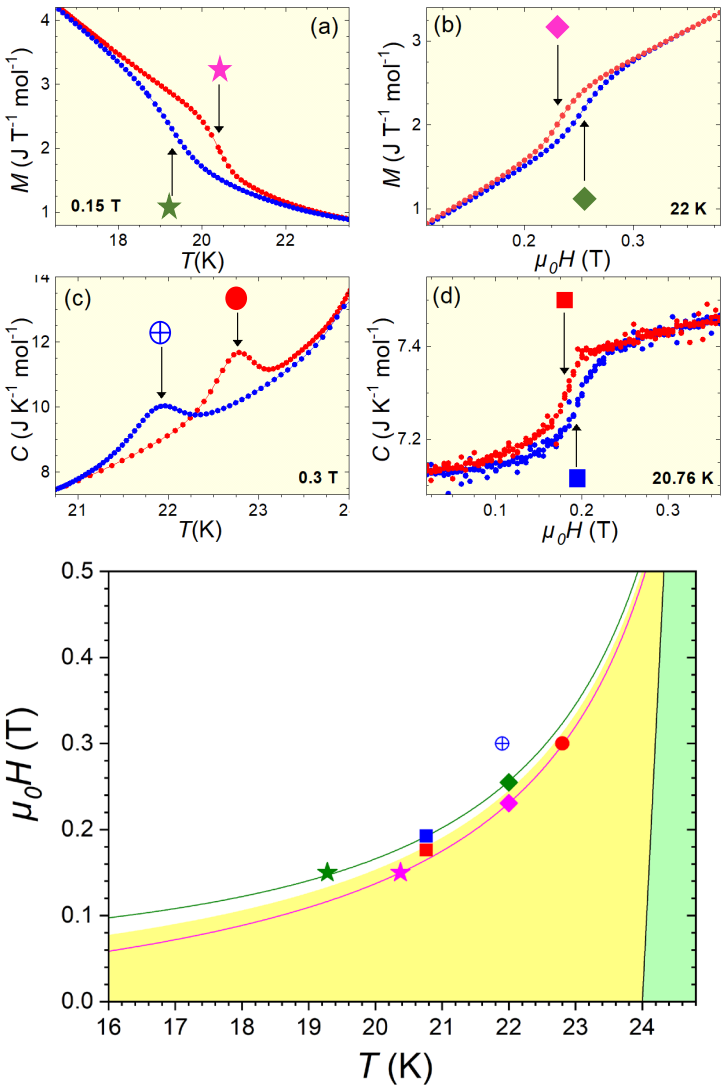

Fig. S3: The upper four panels reproduce the data shown in Fig. 2 of the main text. The locations of the transitions as deduced from the given criteria are marked for each curve. These values are then reported in the phase diagram in the lower panel, where the two lines correspond to the fitted *H*(T)* lines of Fig. 3 in the main text.

Each of the previous measurements was recorded with a certain sweep rate, which was chosen to be very small in order to approach the equilibrium conditions, each time it was possible. These sweep rates were 0.2 K/min for the *M(T)* data and 0.0016 T/min for the *M(H)* curves. The sweep rate was about 0.0004 T/min for the *C(H)* data. The situation is more

complex for the *C(T)* data since one is led to use a single-pulse method. This particular case is described in the manuscript.

It has been reported in the literature that a number of the physical properties of $Ca_3Co_2O_6$ are time dependent. It turns out that this is also the case for the transition line studied here. See, for instance, in Fig S4 the case of *M(H)* at 15 K measured at different sweep rates in an Oxford Instruments vibrating sample magnetometer (VSM).

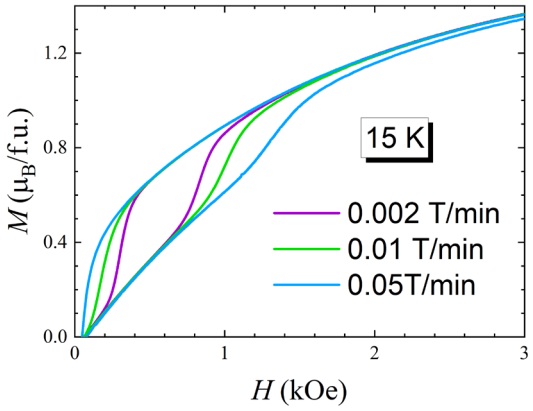

Fig. S4: Low-field part (around *H**) of some hysteresis loops recorded at 15 K with an Oxford Instruments VSM using the different field sweep rates indicated in the legend.

The hysteresis decreases as the sweep rate decreases, while the midpoint of the transition (i.e. *H**) remains approximately the same. These data were recorded using a different crystal and magnetometer to the data discussed in the main text. We note, however, that the lowest sweep rate of 0.002 T/min roughly corresponds to that of the data shown in the main text.

4- Time-resolved analysis of the thermal data

The *C(T)* data of the main text were obtained from a point-by-point analysis of the thermal responses following large heat pulses. Such an approach is required by the first-order nature of the *T*(H)* line. Basically, after a stringent stabilization at a temperature lower than the low-*T* boundary of the transition, a large heat pulse leading the temperature to exceed the high-*T* boundary of the transition is applied. After zeroing the heating power, the temperature returns to its initial value. The two branches are then analyzed independently within the 1τ approximation. Different models have been proposed in the literature, which mainly differ by the way to handle the temperature dependences of all parameters that cannot be neglected over such a wide *T* interval.

We used our approach developed in 2009 which corresponds to the following relationship

$$C(T) = \left[\frac{P(T) - K_w(T)(T - T_0)(1-y)}{(dT/dt)(T)}\right] - C_{ad}(T) \qquad \text{Eq (S1)},$$

where C is the time resolved heat capacity, P the heating power, K_w the thermal conductance of the wires, T_0 the base temperature, C_{ad} the addenda and y is an adjustable parameter (chosen to make these C data overlap with those of the standard 2τ analysis away from the transition). It is clear that the shape of the *C(T)* along each branch is primarily related to the *dT/dt (T)* response.

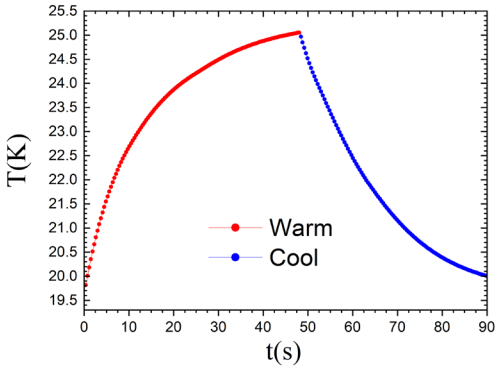

Fig. S5: Thermal response of the platform hosting the $Ca_3Co_2O_6$ sample when submitted to a large heat pulse (data in 0.3 T).

An example of the raw data is shown in Fig. S5. Although hardly perceptible in the overall response, the derivatives reported in Fig. S6a display kinks which are the signatures of the transition (upon warming or cooling). Adding the other parameters with their temperature dependencies in Eq. (S1), one obtains the results of Fig. 6b.

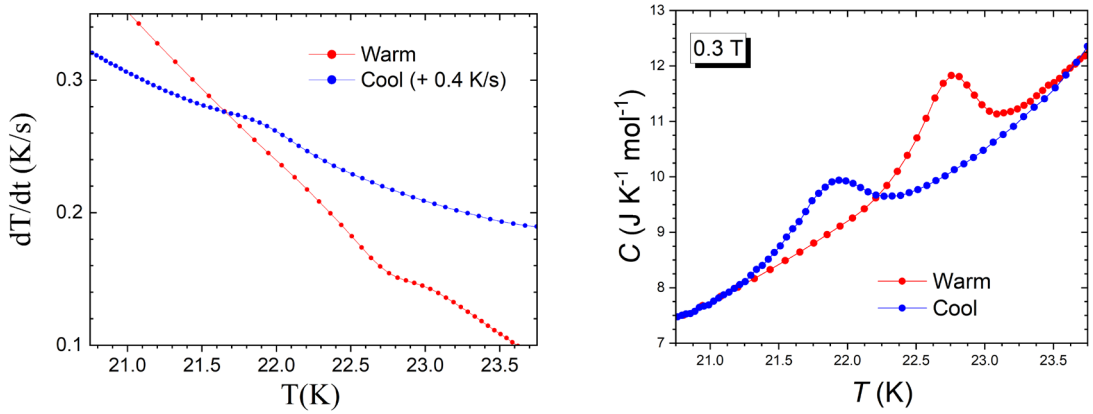

Fig. S6: (a) Derivatives *dT/dt* reported as a function of *T* for both the warming and cooling branches. The latter, which actually corresponds to negative values, has been shifted by adding a constant value to lie in the same range as the former. (b) Final specific heat curves derived from Eq. (S1). The temperature *T* in this 1 τ analysis is that of the platform.

In practice, very similar results can nowadays be obtained using the built-in tool (Single Curve Slope Analysis) incorporated in the recent versions of the Quantum Design Physical Property Measurement System (PPMS) heat capacity option

5- Correction of the temperature lag between the platform and the sample

A sketch of the semi-adiabatic set-up used in the Quantum Design Physical Property Measurement System heat capacity option is shown in Fig. S7.

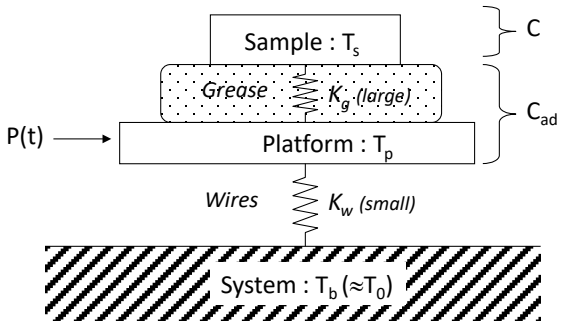

Fig. S7: Operating mode of the PPMS heat capacity option. The thermometer is on the underside of the platform.

There is necessarily a lag between the sample temperature T_s (assumed to be homogeneous owing to the use of thin samples) and the platform temperature T_p. This shift is given by the thermal equation,

$$T_p - T_s = \left[P - C_{ad}\left(dT_p/dt\right) - K_w\left(T_p - T_0\right)\right]/K_g, \qquad \text{Eq. (S2)}$$

where K_g is the thermal conductance of the layer of grease, K_w that of the wires between the platform and the base at temperature T_0, P the heating power applied to the platform, and C_{ad} the heat capacity of the platform plus grease.

The problem is to estimate K_g. An exact analytical resolution of the thermal model of the set-up of Fig. S7 has been developed by Hwang *et al.* [SM1] It is shown that the thermal response $T_p(t)$ resulting from a heat pulse applied to the platform can be fitted by a combination of two exponential functions, characterized by two time constants, a long one and a short one (τ_1 and τ_2, respectively). This is usually called the 2τ model. From Ref. [SM1], we derived an estimate of the grease conductance given by a combination of the two time constants via the relationship

$$K_g = \frac{C_{ad}}{\tau_1\tau_2}\left[(\tau_1 + \tau_2) - \frac{C_{ad}}{K_w}\right] - K_w. \qquad \text{Eq. (S3)}$$

In the same run in which we recorded a series of large pulses at various fields to investigate the first-order transition, we performed standard measurements (heating by 1% of T_p) over a broad T range, that were analyzed by the 2τ model. The time constants τ_1 and τ_2 obtained in this way are shown in the main panel of Fig S8(a), while the inset displays the $C(T)$ derived from the standard 2τ analysis.

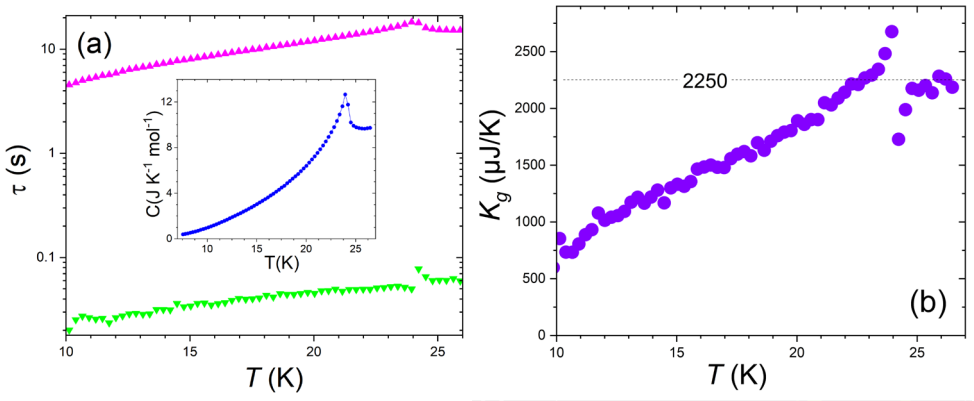

Fig. S8: (a) Time constants and specific heat deduced from the standard method in zero-field. (b) Thermal conductance of the grease layer derived from Eq. 3.

Combining these time constants with the C_{ad} and K_w derived from the background measurements (platform + grease) recorded before installing the sample, one obtains an evaluation of K_g shown in Fig. S8(b). The anomaly visible around 24 K comes from the T_N peak and it must be removed. This curve indicates that K_g within the T-range used for the $T^*(H)$ determination can be approximated by the value 2250 μJ/K.

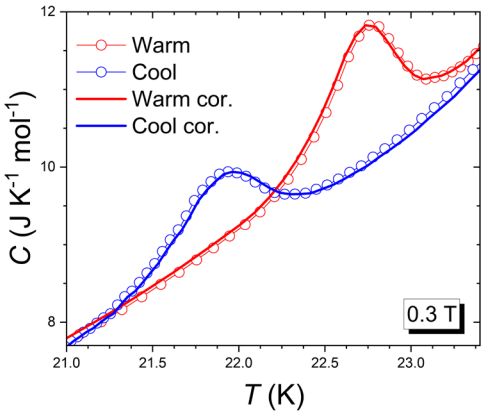

Fig. S9: T^* peaks (upon warming or cooling in 0.3 T) with or without the correction of Eq. (S2). The uncorrected data (open circles) is that plotted versus the measured T_p, while the corrected one (lines) is that plotted versus the calculated T_s.

The correction derived from Eq. (S2) remains small as shown in Fig. S9. Clearly, it cannot account for the offset observed on the $H^*(T)$ line derived from the $C(T_{cool})$ data.

6- Crossover around 13 K in the magnetic response

There is a qualitative change in the shape of the $M(H)$ curves between 14 and 12 K, as shown in Fig. S10. The bubble-like shape of the hysteresis disappears and is replaced by a smoother curve on the field increasing branch and a continuously rounded one on the field decreasing branch, without any sign of metamagnetism at any field.

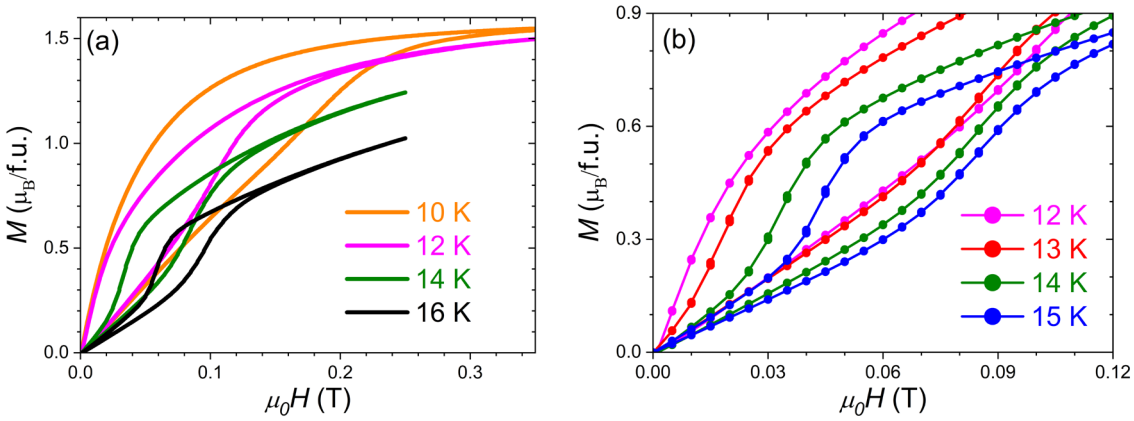

Fig. S10: (a) $M(H)$ curves for $Ca_3Co_2O_6$ with H // c between 10 and 16 K; (b) Enlargement of (a) with 1 K-separated curves confirms that a crossover in behavior takes place around 13 K.

7- Problems with the derivation of T^* from measurements versus T in low fields

In lower fields, the signatures of T^* in the $M(T)$ curves progressively vanish. It disappears first on the cooling branch as shown in Fig. S11(a). The breadth of the hysteresis in temperature at lower fields also ends up making the single-pulse method ineffective below a certain threshold. This is exemplified in Fig. S11(b) by the warming and cooling thermal responses in 0.125 T associated to a large pulse of more than 5 K. It turns out that this pulse remains too small to obtain reliable signatures of T^* in these curves. This limitation cannot be simply overcome by using still larger pulses, since this can induce other technical and analysis problems.

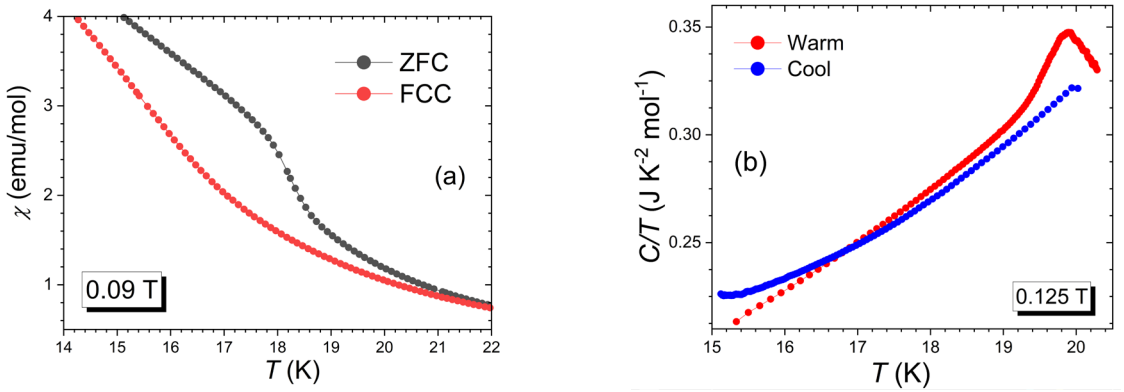

Fig. S11: (a) Magnetic susceptibility in 0.09 T measured upon warming (black circles) or cooling (red circles). (b) Ratio of heat capacity to temperature measured in 0.125 T upon warming (red circles) or cooling (blue circles).

8- Experimental determination of ΔS from specific heat measurements

The determination of ΔS is based on the relationship $\Delta S = \int \frac{C_{exc}(T)}{T} dT$, where C_{exc} is the excess specific heat associated with the latent heat, and the integration is performed over the

whole width of the transition peak. The excess specific heat is obtained by subtracting a baseline which reflects the background not affected by the magnetic transition. This $C_{bas}(T)$ can be accurately measured outside of the transition region by using the standard 2τ model (the data within the transition region must be discarded since it can be distorted by the latent heat peak). It turns out that this $C_{bas}(T)$ evolves substantially with the magnetic field as visible in Fig. S12(a).

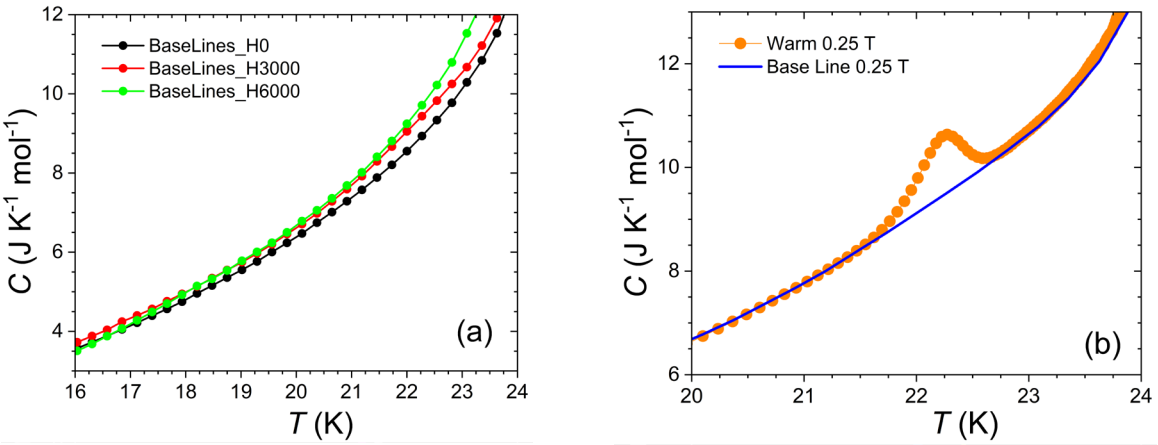

Fig. S12: (a) Baselines derived from standard 2τ measurements in 0, 0.3 and 0.6 T; (b): Example of the relative positioning between a T^* peak and its corresponding baseline (case of 0.25 T).

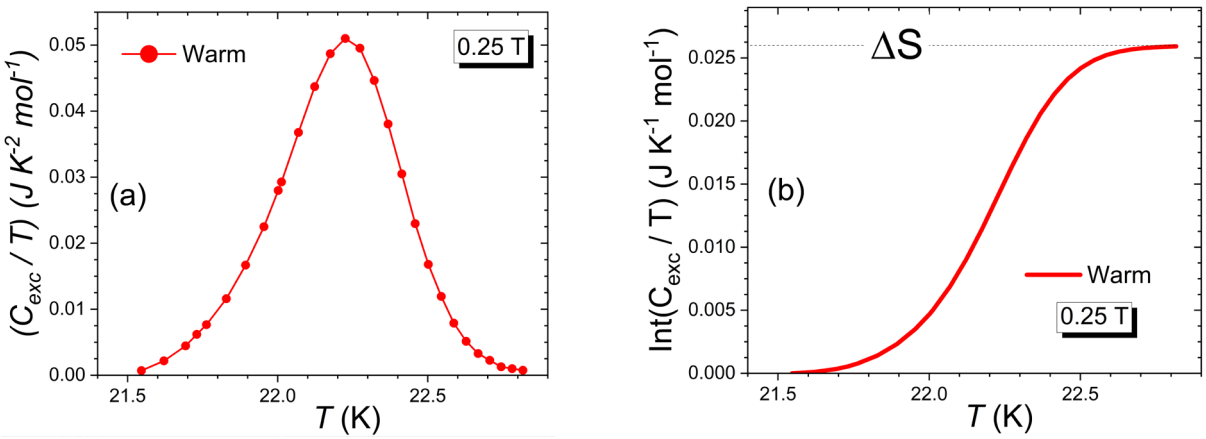

Fig. S13: (a) Ratio of the excess heat capacity to temperature around the transition in 0.25 T; (b) Integration of $C_{exc}/T(T)$ across the transition; the saturation value reflects the entropy jump ΔS.

The overall process to obtain ΔS is exemplified in the case of $\mu_0 H = 0.25$ T upon warming. Fig. S12(b) shows the $C(T_{warm})$ obtained from a large pulse, as well as the $C_{bas}(T)$ derived from the standard method. The difference between these curves yields $C_{exc}(T)$. Fig. S13(a) displays this C_{exc}/T curve, while Fig. S13(b) shows its integration over the transition width. The ΔS is the saturation value of this integration.

9- Experimental determination of ΔS from magnetization measurements

At a first-order transition, the entropy change can be estimated from Clausius-Clapeyron relationships. Its magnetic version reads $\Delta S = -\mu_0 \Delta M / (\frac{dT^*}{\mu_0 dH})$. From linear approximations of the $M(H)$ curve on each side of the transition, one can estimate the step ΔM by considering the shift between these two extrapolations at the level of the transition midpoint. This method is illustrated in Fig. S14(a) in the case of $T = 22$ K.

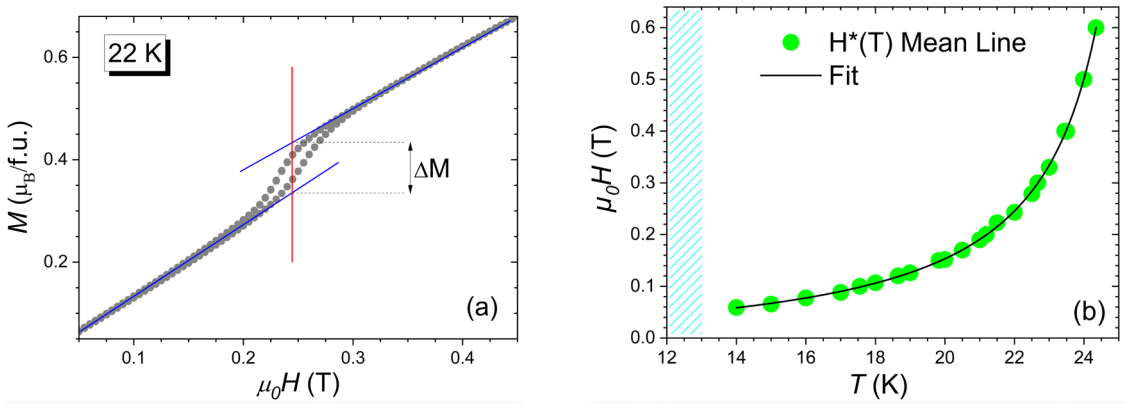

Fig. S14: (a) Magnetization curve at 22 K showing the construction used to evaluate the magnetization step at the transition; (b) Transition line in the (H, T) plane with its fitting by the expression $H = H_0 + \frac{aT^b}{(c-T)}$.

In our analysis, we associate ΔM to the mean transition i.e. ($H_C Up$ + $H_C Down$)/2 or ($T_C Warm$ + $T_C Cool$)/2. This "mean line" $H^*(T)$ shown in Fig. S14(b) can be fitted to the phenomenological expression $H = H_0 + \frac{aT^b}{(c-T)}$. Incorporating ΔM and the calculated dT^*/dH in the Clausius-Clapeyron equation, one obtains a value $\Delta S = 0.034$ J K^{-1} mol^{-1} for $T = 22$ K.

10- Transition field towards saturation at $T << T_N$

At low temperature (but above the multiple-steps regime, i.e. roughly 5 $< T <$ 15 K) the $M(H)$ curves of $Ca_3Co_2O_6$ exhibit a FR plateau (at $M_{sat}/3$) followed by a jump towards full saturation. This is illustrated in Fig. S15 for the case of $T = 10$ K (data from Ref. [6]). The point of largest slope along this transition is found at 3.6 T. This field $\mu_0 H_{sat}$ also corresponds to the third step along the multi-step response at $T < 5$ K.

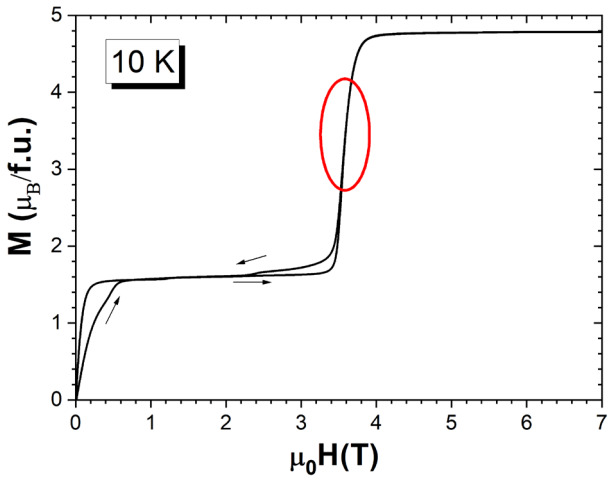

Fig. S15: *M(H)* cycle recorded at 10 K. The arrows indicate the direction of the field variation, while the red ellipse highlights the jump towards saturation that takes place around $\mu_0 H_{sat}$ = 3.6 T.

In Fig. S15 (taken from a previous study carried out on another batch of crystals), we found M_{sat} ~ 4.8 μ_B / f.u. However the greater part of our data have led to slightly larger values of the order of 5 / f.u. Widening the scope to the results reported by different research teams, one obtains a mean value of M_{sat} close to 5.2 μ_B / f.u. [17,18, 25].

11- Possible scenario for the field dependence of the SDW state

Following the results of neutron diffraction in $PrNi_2Si_2$ [40,41], Fig S16 illustrates what we proposed to be the field-induced evolution of the spin structure of each chain in $Ca_3Co_2O_6$ (for the sake of clarity, the spins are shown perpendicular to the chains, while they are actually parallel the chains). One starts from a pure sinusoid in zero-field, which is progressively shifted along the field direction as the field is increased, leading to a reduction in the modulation amplitude. Since the field makes the spin phase evolve towards ferrimagnetism, one can consider that two of the three chains follow this evolution with a net positive magnetization (i.e. parallel to the field), whereas the magnetization is negative (antiparallel to the field) for the third chain. This process ends by a sudden switch to an unmodulated phase, taking place at a critical field that we associate to H^*. This scenario would be compatible with our magnetic and calorimetric data in $Ca_3Co_2O_6$. However, investigations by neutron diffraction or other techniques will be necessary to clarify this scenario in the case of $Ca_3Co_2O_6$.

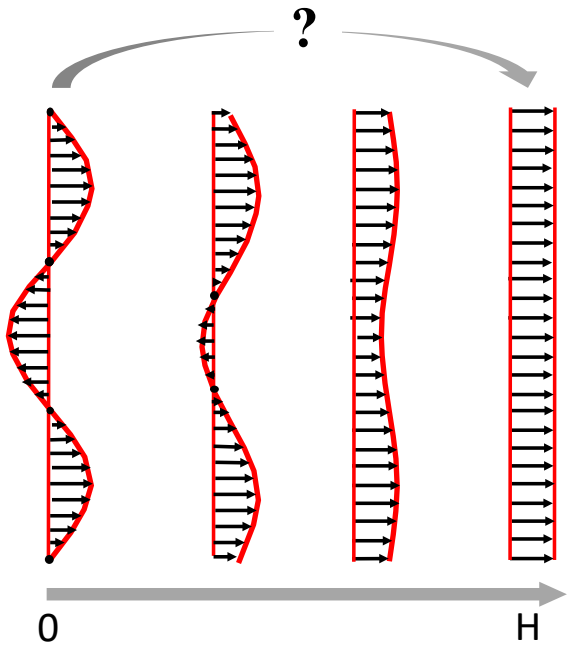

Fig. S16: Suggested evolution of the SDW versus field applied along the spin direction (the spins are drawn perpendicular to the chains for clarity, while they are actually parallel to the chains). There is a consensus view about the nature of the start and end states, but the transformation between them is still under debate. In our vision, H^* corresponds to a jump between the last two states on the right.

[SM1] J. S. Hwang, K. J. Lin, and C. Tien, *Measurement of heat capacity by fitting the whole temperature response of a heat-pulse calorimeter*, Rev. Sci. Instrum. **68**, 94 (1997).